Astronomy & Astrophysics

Fast magnetoacoustic waves in curved coronal loops

II. Tunneling modes

E. Verwichte, C. Foullon, and V. M. Nakariakov

Department of Physics, University of Warwick, Coventry CV4 7AL, UK
e-mail: Erwin.Verwichte@warwick.ac.uk

ABSTRACT

Aims. Fast magnetoacoustic waves in curved coronal loops are investigated and the role of lateral leakage in wave damping, which includes the mechanism of wave tunneling, is explored.
Methods. A coronal loop is modeled as a curved, magnetic slab in the zero plasma-β limit. In this model and for an arbitrary piece-wise continuous power law equilibrium density profile, the wave equation governing linear vertically polarised fast magnetoacoustic waves is solved analytically. An associated dispersion relation is derived and the frequencies and eigenfunctions of the wave modes are characterised.
Results. For some equilibria, the waves are shown to be all damped due to lateral leakage. It is demonstrated that waves either leak straight out into the external medium or have to overcome an evanescent barrier, which is linked to wave tunneling. The wave solutions consist of alternating vertically polarised kink and sausage branches. Fast kink oscillations may have a non-zero density perturbation when averaged across the loop. The calculated damping rate of fast magnetoacoustic kink oscillations is shown to be consistent with related numerical simulations and show that lateral leakage may explain the observed damping of (vertically polarised) fast magnetoacoustic kink oscillations.

Key words. Sun: oscillations – magnetohydrodynamics (MHD)

1. Introduction

In recent years, magnetohydrodynamical (MHD) waves and oscillations in the solar corona have been successfully identified in observations from ground-based and space-born instruments. In particular, fast magnetoacoustic kink oscillations in coronal loops have received a great deal of attention (see e.g. Nakariakov & Verwichte 2005, for a review).

The role of curvature on the behaviour of MHD waves in coronal loops has been addressed by a number of authors, as reviewed in Verwichte et al. (2006a). Recently, Brady & Arber (2005) performed numerical simulations of vertically polarised fast magnetoacoustic kink oscillations in a coronal loop modeled as a curved magnetic slab, which is particularly relevant for vertically polarised kink oscillations. They found that oscillation damping times due to lateral leakage is of the same order as the observed damping time reported by Wang & Solanki (2004). Furthermore, they explained the leakage as wave tunneling through an evanescent barrier above the coronal loop. Curvature is actually not essential for the occurrence of wave tunneling, provided a non-piece-wise constant profile for the Alfvén speed is considered (Brady et al. 2006), but the curved geometry does allow for wave leakage through tunneling even if the Alfvén speed profile is piece-wise constant.

In Verwichte et al. (2006a), here after denoted Paper I, we introduced an analytical model for vertically polarised fast magnetoacoustic waves in a curved coronal loop, in the zero plasma-β limit, where the role of the index of the piece-wise continuous power law density profile was discussed. It was shown that for the considered equilibria, except for one special case, fast waves are no longer trapped in the loop and leak out into the external medium. Also, For the particular case, corresponding to a piece-wise constant Alfvén frequency profile, for which fast waves are trapped, we explicitly solved the governing wave equation and found that the mode frequencies do not differ substantially from the straight slab loop model of Edwin & Roberts (1982). However, in the curved loop model, the fast kink oscillations may have significant density perturbations.

The other cases of density profiles, which involve non-trapped waves, are now the subject of this paper. The paper is structured as follows. In Sect. 2, the coronal loop model and the governing wave equation, also used in Paper I, are briefly introduced, and solved for the studied cases. In Sect. 3, the types of wave modes are classified. In Sect. 4, the dispersion relation is derived and its eigenmodes and eigenfrequencies are examined. The mechanism of leakage by wave tunneling is investigated in Sect. 5 and its efficiency as a damping mechanism is discussed in Sect. 6.
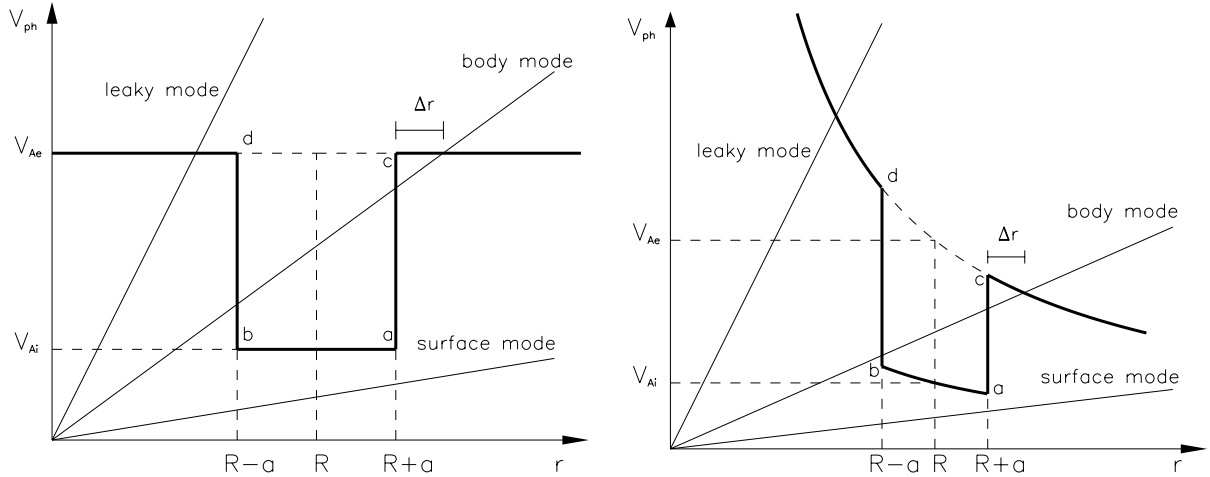
Fig. 1. Alfvén speed profile as a function of r, corresponding to Eq. (2) with (*left*) $\alpha = -2$ and (*right*) $\alpha = 0$. The letters a, b, c, d show the phase speeds V_{pha}, V_{phb}, V_{phc} and V_{phd}. The phase speeds of three wave scenarios corresponding to surface, body and leaky modes are shown. The location and width Δr of the evanescent barrier is shown.

2. Model and governing equations

The coronal loop is modeled, in the zero plasma-β limit, as a semi-circular slab of half-width a and radius of curvature R, which is line-tied at the solar surface with rigid boundary conditions. We use a cylindrical coordinate system with origin at the centre of curvature of the slab, at the solar surface. The slab and the equilibrium magnetic field are directed along the azimuthal ϕ-direction, with the solar surface located at $\phi = [0, \pi]$. The z-direction is parallel to the solar surface and perpendicular to the loop axis. In the radial direction, with coordinate r, the semi-infinite space is partitioned into a lower external ($r < R - a$), internal ($R - a \leq r \leq R + a$) and upper external ($r > R + a$) region (see Fig. 1 of Paper I for an illustration of the model). The azimuthal equilibrium magnetic field is of the form $\boldsymbol{B_0} = B_0(r/R)^{-1}$. Gravity has been neglected. The equilibrium density is a piece-wise continuous power law of the form

$$\rho_0(r) = \begin{cases} \rho_{0\mathrm{i}} \left(\frac{r}{R}\right)^{\alpha} & |r - R| \leq a \\ \rho_{0\mathrm{e}} \left(\frac{r}{R}\right)^{\alpha} & |r - R| > a, \end{cases} \tag{1}$$

where the constants $\rho_{0\mathrm{i}}$ and $\rho_{0\mathrm{e}}$ are the values of the internal and external density profiles at $r = R$, respectively. The index α determines the shape of the density profile. The case $\alpha = -4$ was studied in detail in Paper I. Here, the cases $\alpha \neq -4$ are investigated. The Alfvén speed profile is of the form

$$V_{\mathrm{A}}(r) = \begin{cases} V_{\mathrm{Ai}} \left(\frac{r}{R}\right)^{-\frac{\alpha+2}{2}} & |r - R| \leq a \\ V_{\mathrm{Ae}} \left(\frac{r}{R}\right)^{-\frac{\alpha+2}{2}} & |r - R| > a, \end{cases} \tag{2}$$

where the constants V_{Ai} and V_{Ae} are the values of the Alfvén speed at $r = R$ for the internal and external density profiles respectively. The ratio $V_{\mathrm{Ai}}/V_{\mathrm{Ae}}$ is equal to $\sqrt{\chi}$, where $\chi = \rho_{0\mathrm{e}}/\rho_{0\mathrm{i}}$ is a measure of the density contrast and for a coronal loop this parameter is typically less than unity.

We consider vertically polarised fast magnetoacoustic oscillations with a radial displacement, ξ_r, Eulerian magnetic pressure perturbation, P, and Eulerian density perturbation,

ρ of the form $f = \hat{f}(r) \sin(m\phi) \exp(-\mathrm{i}\omega t)$, where ω is the angular frequency of a mode of azimuthal degree m. In order for the wave mode to fulfil the boundary conditions at $\phi = 0, \pi$, m needs be an integer. Later in the paper we shall regularly use m as a real number for the sake of mathematical clarity. It has to be born in mind, though, that only wave solutions with integer degrees m are physical.

The governing wave equation for the radial displacement is (see Paper I)

$$\left[\frac{\mathrm{d}^2}{\mathrm{d}r^2} + \frac{1}{r}\frac{\mathrm{d}}{\mathrm{d}r} + \left(\frac{\omega^2}{V_{\mathrm{A}}^2(r)} - \frac{m^2}{r^2} \right) \right] \left(\frac{\hat{\xi}_r}{r} \right) = 0. \tag{3}$$

The last term of Eq. (3) can be seen as the square of the "radial component" of the wave vector.

For a density profile proportional to r^{α}, the general solution to Eq. (3), with $\alpha \neq -4$, in the internal region, is given by

$$\left(\frac{\hat{\xi}_r}{r} \right) = \sum_{m=1}^{\infty} A_{\mathrm{i},m} J_{\nu}(\Omega s) + B_{\mathrm{i},m} Y_{\nu}(\Omega s), \tag{4}$$

where

$$s = \frac{1}{|\delta|} \left(\frac{r}{R} \right)^{\delta}, \quad \delta = \frac{\alpha+4}{2}, \quad \nu = \left| \frac{m}{\delta} \right|, \quad \Omega = \frac{\omega R}{V_{\mathrm{Ai}}}. \tag{5}$$

Ω is the dimensionless frequency. Integration constants $A_{\mathrm{i},m}$ and $B_{\mathrm{i},m}$ are dimensionless displacement amplitudes, which may be complex. The functions J_{ν} and Y_{ν} are the Bessel and Neumann functions of real order ν.

The magnetic pressure and density perturbations are respectively given by

$$\left(\frac{\hat{P}}{P_0} \right) = -2r \frac{\mathrm{d}}{\mathrm{d}r} \left(\frac{\hat{\xi}_r}{r} \right), \tag{6}$$

and

$$\left(\frac{\rho}{\rho_0} \right) = \frac{1}{2} \frac{P}{P_0} - 2 \frac{\xi_r}{r} - \alpha \frac{\xi_r}{r}. \tag{7}$$

P_0 is the equilibrium magnetic pressure. The Eulerian density perturbation consists of three contributions. The first term is

due to the magnetic pressure perturbation and is present in straight coronal loop models (e.g. Edwin & Roberts 1982). The second term is associated with the loop curvature and is connected with the perturbation of the loop length (and hence also loop volume). The third term is due to the advection of the inhomogeneous equilibrium density and reflects the difference between the Eulerian and Lagrangian descriptions. The Lagrangian density perturbation, which is relevant when comparing to observations, is given by

$$\left(\frac{\delta\rho}{\rho_0}\right) = \frac{\rho}{\rho_0} + \frac{1}{\rho_0}(\boldsymbol{\xi}.\boldsymbol{\nabla})\rho_0 = \frac{1}{2}\frac{P}{P_0} - 2\frac{\xi_r}{r}. \tag{8}$$

Here we shall examine in detail the cases with α larger than -4 ($\delta > 0$). These cases involve wave leakage into the upper external medium. The cases with α smaller than -4 ($\delta < 0$), which involve wave leakage into the lower external medium, are less realistic as they are associated with steeply decreasing density profiles. We briefly discuss these cases in the Appendix.

3. Wave mode classification

In our curved slab model, the azimuthal (or longitudinal) wavelength of a wave mode has to increase linearly with radial distance in order for the wave to remain in phase in the radial direction. Therefore, the longitudinal oscillation phase speed is given by $V_{ph}(r) = \Re\omega r/m$, where $\Re\omega$ is the real part of the oscillation frequency. Where the phase speed is above (below) the Alfvén speed, the solution is said to be "oscillatory" ("evanescent"). This behaviour can be seen in the sign of the last term of Eq. (3), although this is not reflected in the mathematical form of the wave solution. The propagatory behaviour of the wave determines the choice of boundary conditions at $r = 0$ and $r \to \infty$ and hence the choice of external solutions. As discussed in Paper I, the cases with $\alpha > -4$ represent an Alfvén speed profile which the phase speed $V_{ph}(r)$ crosses from below, so that the solution is evanescent for small r and oscillatory for large r. Therefore, waves cannot remain trapped inside the loop and will leak into the upper external region. Figure 1 shows Alfvén speed profiles for a model with a piece-wise constant Alfvén speed ($\alpha = -2$) and a model with a piece-wise constant equilibrium density ($\alpha = 0$).

A characteristic phase speed of a mode is its value at the slab axis, i.e. $V_{ph}(R) = \Re\Omega V_{Ai}/m$. Also, we define the wave period $P = 2\pi/\Re\omega$ and the damping time $\tau = -1/\Im\omega$. The Alfvén speed profile has four points, which are important for understanding the propagatory behaviour of a wave mode. Those points are denoted a, b, c, d as highlighted in Fig. 1 and correspond to (a) upper internal, (b) lower internal, (c) upper external and (d) lower external edges of the slab. Where the phase speed $V_{ph}(r)$ matches the Alfvén speed in those points, $V_{ph}(R)$ takes the respective values

$$V_{pha} = V_{Ai}\left(1 + \frac{a}{R}\right)^{-\delta}, \qquad V_{phb} = V_{Ai}\left(1 - \frac{a}{R}\right)^{-\delta},$$
$$V_{phc} = \frac{V_{Ai}}{\sqrt{\chi}}\left(1 + \frac{a}{R}\right)^{-\delta} \quad \text{and} \quad V_{phd} = \frac{V_{Ai}}{\sqrt{\chi}}\left(1 - \frac{a}{R}\right)^{-\delta}. \tag{9}$$

V_{pha} and V_{phd} are always the smallest and largest speeds respectively, viz. $V_{pha} \le V_{Ai} < V_{Ae} \le V_{phd}$. V_{phb} and V_{phc} are always intermediate between V_{Ai} and V_{Ae}. The ordering between V_{phb}
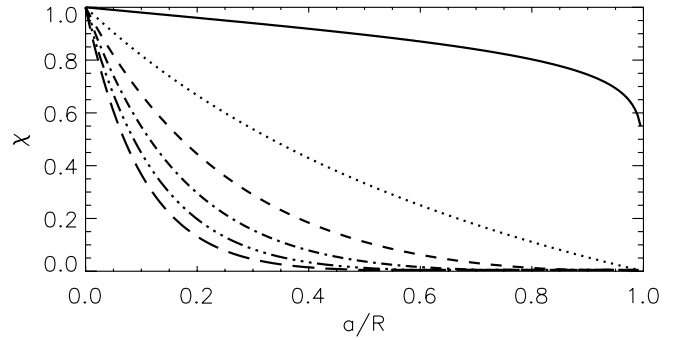

Fig. 2. Regimes in parameter space of a/R and χ for which V_{phb} is smaller (below the curve) or larger (above the curve) than V_{phc} for six values of α: -3.9 (solid), -3.0 (dotted), -2.0 (dashed), -1.0 (dot-dashed), 0.0 (triple dot-dashed) and 1.0 (long-dashed). Body tunneling modes may only exist if $V_{phb} < V_{phc}$.

and V_{phc} depends on the parameters a/R and χ. Figure 2 shows the regimes in parameter space for which V_{phb} is either smaller or larger than V_{phc}. If a/R and χ are small, then $V_{phb} < V_{phc}$ and vice-versa. In the upper limit of $\alpha \to -4$, the speeds V_{pha} and V_{phb} tend to V_{Ai}, and V_{phc} and V_{phd} tend to V_{Ae}.

A wave mode can be classified based on the propagatory behaviour at the upper external interface (c), $r = R + a$. If $V_{ph}(R) < V_{phc}$, modes are evanescent in the upper external region in the immediate vicinity of the slab, but become oscillatory further away. This evanescent barrier is characteristic of wave tunneling and therefore we call such modes *tunneling modes*. The exact width of the evanescent barrier, Δr, can be calculated using geometrical considerations. It is equal to $\Delta r = r_c - (R + a)$, with r_c, the upper end of this barrier, which is defined as the distance where the phase speed $V_{ph}(r)$ matches the Alfvén speed in the upper external region (see Fig. 1 for an illustration):

$$\left(\frac{r_c}{R}\right) = \left(\frac{V_{ph}(R)}{V_{Ae}}\right)^{-1/\delta} = \left(\sqrt{\chi}\frac{\Re\Omega}{m}\right)^{-1/\delta}, \tag{10}$$

which is equivalent to

$$r_c = \left(\frac{V_{ph}(R)}{V_{phc}}\right)^{-1/\delta}(R + a). \tag{11}$$

This expression confirms that an evanescent barrier exists ($r_c > R + a$) only if $V_{ph}(R) < V_{phc}$. Wave modes with $V_{ph}(R) \ge V_{phc}$ are oscillatory in the whole upper external region and the wave can leak straight nto the external region. We call such modes *leaky modes*. Note that tunneling and leaky type modes are modes that both inherently leak wave energy into the external medium. The name "leaky" is used here specifically for those modes, which do not propagate through an evanescent barrier.

Similar to the trapped modes in a straight coronal loop model (e.g. Edwin & Roberts 1982, 1983), the wave modes with $V_{ph}(R) \le V_{phd}$ may also be classified into surface or body (hybrid surface-body modes are also possible) depending whether such modes are evanescent and/or oscillatory inside the slab. However, this classification is of lesser importance as it does not affect the mathematical form of the solution.
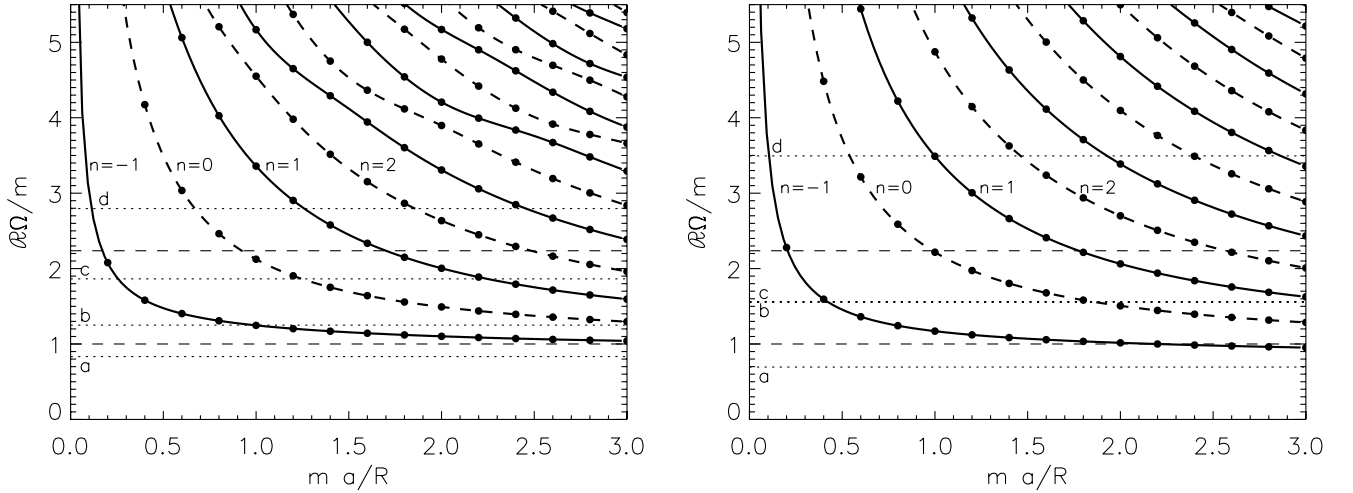
Fig. 3. (*Left*) Dispersion diagram showing the normalised phase speeds $\Re\Omega/m = V_{\text{ph}}(R)/V_{\text{Ai}}$ of the solutions of dispersion relation (14) as a function of ma/R, for waves in a curved loop model with a piece-wise constant Alfvén speed profile ($\alpha = -2$). The thick solid and dashed lines are the solution branches for the kink and sausage modes respectively. The first four branches are annotated. The circles denote physical solutions with integer values of m. The parameters $\chi = 0.2$ and $a/R = 0.2$. The position where $V_{\text{ph}}(R) = V_{\text{Ai}}$ and $V_{\text{ph}}(R) = V_{\text{Ae}}$ are shown with thin dashed lines. The locations of V_{pha}, V_{phb}, V_{phc} and V_{phd} are shown with thin dotted lines and annotated with the corresponding letter. (*Right*) Same diagram for a curved loop model with a piece-wise constant density profile ($\alpha = 0$).

4. Wave mode characteristics

4.1. Dispersion relation

We impose the boundary conditions that $\hat{\xi}_r$ vanishes at $r = 0$ and that for $r \to \infty$ only the solution that propagates in the positive r-direction, away from the slab, is permitted. The solutions for $\hat{\xi}_r$ and $\hat{P}$ for one mode of degree m that obey these boundary conditions are given by

$$\left(\frac{\hat{\xi}_r}{r}\right) = \begin{cases} A_{\text{e}} \, J_\nu(\sqrt{\chi}\Omega s) & r < R - a \\ A_{\text{i}} \, J_\nu(\Omega s) + B_{\text{i}} \, Y_\nu(\Omega s) & |r - R| \leq a \\ B_{\text{e}} \, H_\nu^{(1)}(\sqrt{\chi}\Omega s) & r > R + a, \end{cases} \quad (12)$$

$$\left(\frac{\hat{P}}{P_0}\right) = -2r \begin{cases} A_{\text{e}} \frac{\text{d}}{\text{d}r} J_\nu(\sqrt{\chi}\Omega s) & r < R - a \\ A_{\text{i}} \frac{\text{d}}{\text{d}r} J_\nu(\Omega s) + B_{\text{i}} \frac{\text{d}}{\text{d}r} Y_\nu(\Omega s) & |r - R| \leq a \\ B_{\text{e}} \frac{\text{d}}{\text{d}r} H_\nu^{(1)}(\sqrt{\chi}\Omega s) & r > R + a, \end{cases} \quad (13)$$

where $H_\nu^{(1)}$ is the first Hankel function of order ν. The continuity of the displacement, $\hat{\xi}_r$, and the Lagrangian total pressure perturbation, $\delta\hat{P} = \hat{P} - 2P_0\hat{\xi}_r/r$, at $r = R \pm a$ leads to the dispersion relation

$$\frac{\mathcal{W}\{J_\nu(\Omega s_-), J_\nu(\sqrt{\chi}\Omega s_-)\}}{\mathcal{W}\{Y_\nu(\Omega s_-), J_\nu(\sqrt{\chi}\Omega s_-)\}} = \frac{\mathcal{W}\{J_\nu(\Omega s_+), H_\nu^{(1)}(\sqrt{\chi}\Omega s_+)\}}{\mathcal{W}\{Y_\nu(\Omega s_+), H_\nu^{(1)}(\sqrt{\chi}\Omega s_+)\}}, \quad (14)$$

where $\mathcal{W}\{f(x), g(y)\} = f(x)\frac{\text{d}g}{\text{d}r}(y) - \frac{\text{d}f}{\text{d}r}(x)g(y)$ and $s_\pm = (1 \pm a/R)^\delta/|\delta|$. In addition to the azimuthal wave number m, the dispersion relation depends explicitly on three other parameters: χ, the density contrast, a/R, the loop aspect ratio, and the power law index α that characterises the equilibrium density profile. Since wave modes are to be damped, we expect the imaginary part of the mode frequency, $\Im\omega$, to be negative.

4.2. Eigenmodes

Dispersion relation (14) is solved for Ω as a function of m, where real (not just integer) values of m are taken for mathematical clarity. Figure 3 shows dispersion diagrams showing the real and imaginary parts of the solutions for two values of α. We choose to plot the dispersion diagrams as a function of ma/R, which is the equivalent for this model of ka used by Edwin & Roberts (1982, 1983) in straight loop models (k is the longitudinal component of the wave vector in cartesian geometry). All modes are either body or hybrid surface-body modes. Surface modes do not exist and this is also found for the straight magnetic slab model of Edwin & Roberts (1982).

Figure 3 shows an alternation of fast magnetoacoustic kink and sausage mode "branches", ridges of harmonics in the radial direction. Following the notation introduced in Paper I, the mode branches are denoted by an integer n, where even and odd values of n refer to sausage and kink modes respectively. The fundamental kink branch is denoted by $n = -1$.

In the short wavelength limit ($m \to \infty$), we observe that the phase speed of the wave modes, $V_{\text{ph}}(R)$, of all branches tends to V_{pha}. This speed is a function of the loop aspect ratio (see Eq. (9)) such that thick loops have a lower limit phase speed than thin loops. In the long wavelength limit ($m \to 0$), we observe that all mode branches have a phase speed tending to infinity. This is in contrast with the case investigated in Paper I and the straight slab model where the phase speed of the fundamental kink branch ($n = -1$) tends to V_{Ae}. Therefore, the phase speed of the fundamental kink mode ($n = -1$) in this model of coronal loops cannot be approximated by its long wavelength limit as is often done when a loop is modeled as a straight slab or cylinder (e.g. Roberts et al. 1984).

Trapped modes, which typically exist in the straight slab model (Edwin & Roberts 1982), are not present here. This manifests itself by wave damping of every mode (see Fig. 4).
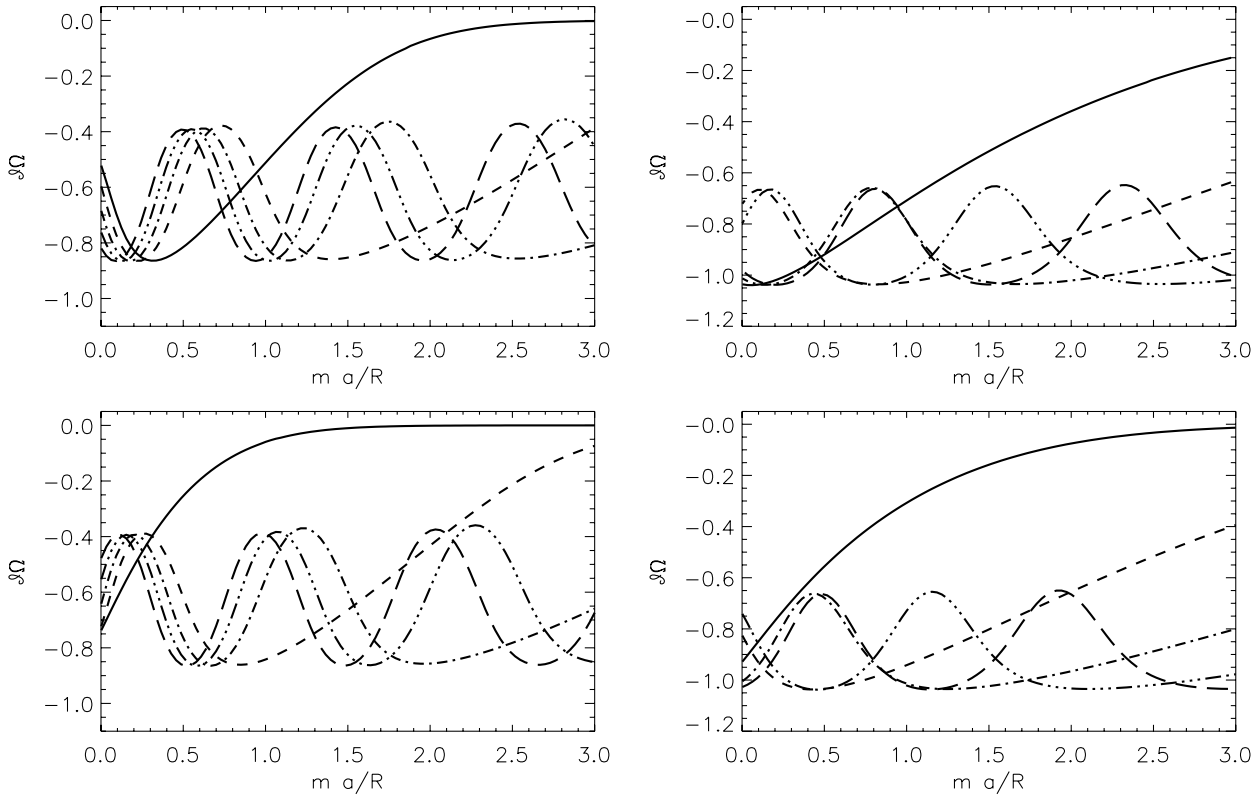
Fig. 4. (*Left*) Dispersion diagram showing the imaginary part of the wave mode frequency, $\Im\Omega$, of the solutions of dispersion relation (14) as a function of ma/R for a curved loop model with a piece-wise constant Alfvén speed profile ($\alpha = -2$). (*Top*) Sausage modes, where the curves correspond to the solution branches n: 0 (solid), 2 (dashed), 4 (dot-dashed), 6 (triple dot-dashed) and 8 (long dashed). (*Bottom*) Kink modes, where the curves correspond to the solution branches n: -1 (solid), 1 (dashed), 3 (dot-dashed), 5 (triple dot-dashed) and 7 (long dashed). The parameters $\chi = 0.2$ and $a/R = 0.2$. (*Right*) Same diagrams for a curved loop model with a piece-wise constant density profile ($\alpha = 0$).

In the short wavelength limit, we observe that the damping rate tends to zero. Such damping behaviour would be expected in the case of an infinite evanescent barrier. Yet, the upper end of the evanescent barrier tends to a finite value $r_c \rightarrow R(\sqrt{\chi}V_{\mathrm{pha}})^{-1/\delta}$. We can understand this by considering that the rate of wave damping due to tunneling is typically of the form $\Im\omega \sim -\mathrm{e}^{-Ck_r\Delta r}$, where C is a constant and k_r represents the "radial component" of the wave vector and is related to the wave frequency approximated by the dispersion relation for fast waves, i.e. $\omega \approx V_{\mathrm{A}}(k_r^2 + m^2/r^2)^{1/2}$ (e.g. Brady et al. 2006). Because the phase speed tends to the constant V_{phc} as m tends to infinity, $\Im\omega \sim -\mathrm{e}^{-C'm\Delta r}$, where C' is a constant with respect to m. This shows that the damping rate is determined by the product of the evanescent barrier width and the azimuthal degree, so that even if Δr remains finite, $m\Delta r$ tends to infinity in the short wavelength limit and the damping rate tends to zero. Figure 5 shows the damping time τ as a function of the product $m\Delta r$ for the fundamental kink branch ($n = -1$). The damping time in the regime of tunneling modes ($\Delta r > 0$) is reasonably approximated by an exponential.

Figure 6 shows the radial structure of the Eulerian perturbation quantities of the fundamental sausage and kink modes. Figure 7 visualises the perturbation of the curved loop by the fundamental sausage and kink modes with the density perturbation given by Eq. (8). The sausage mode is a symmetric solution, which displaces the loop boundaries in opposite
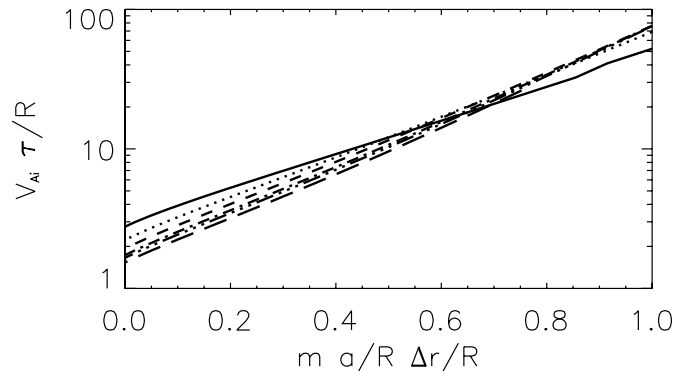

Fig. 5. Dimensionless damping time $V_{\mathrm{Ai}}\tau/R$ as a function of $(ma/R)(\Delta r/R)$ for the fundamental kink mode branch ($n = -1$) and various values of α: -2.8 (solid), -2.0 (dotted), -1.2 (dashed), -0.4 (dot-dashed), 0.0 (triple dot-dashed) and 0.8 (long dashed). The parameters $\chi = 0.2$ and $a/R = 0.2$.

directions, away from and towards the slab axis. The displacement has a node near the slab axis. The constants A_i and B_i are determined by prescribing the displacement at the inner boundary to be $\hat{\xi}_r(R - a) = (R - a)A$, where A is the normalised displacement amplitude. The kink mode is an anti-symmetric solution, which displaces the loop boundaries in the same direction, upwards or downwards. The displacement has an anti-node near the slab axis. The constants A_i and B_i are
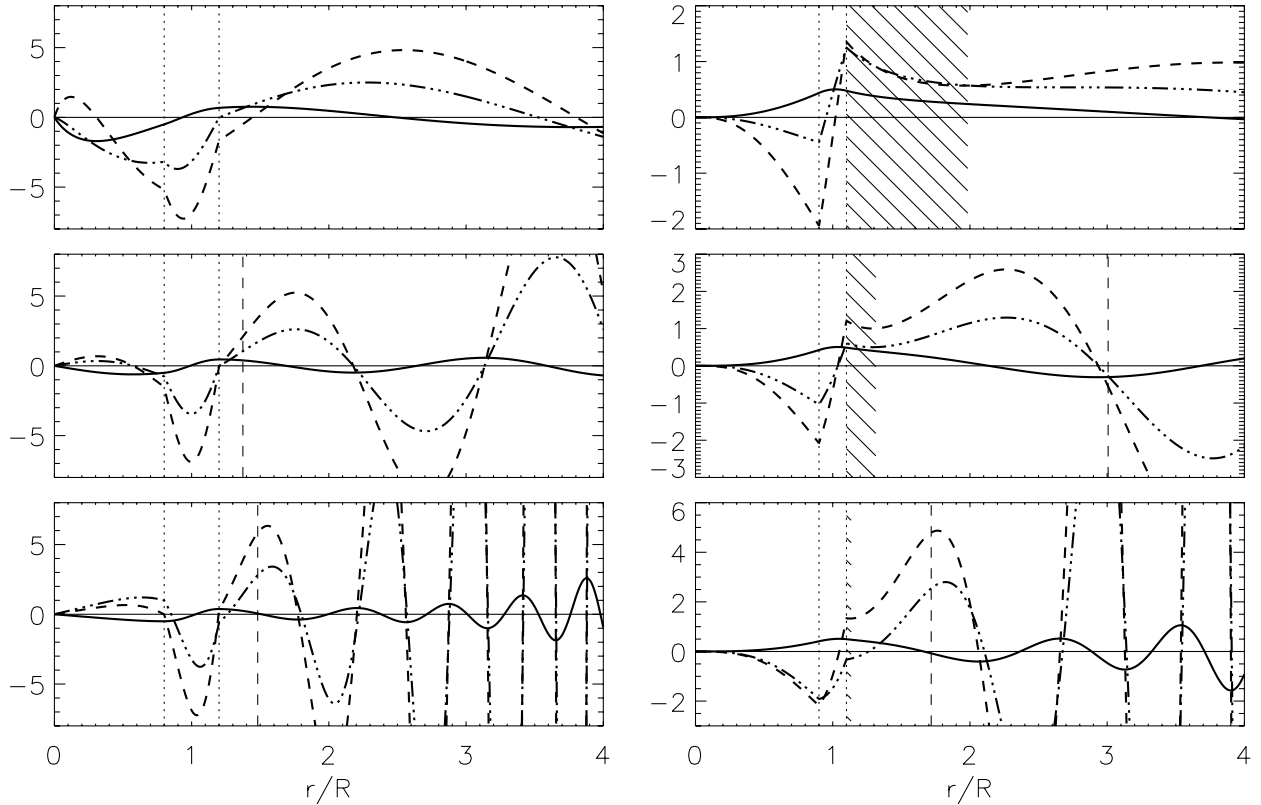
Fig. 6. (*Left*) Real part of the quantities $\hat{\xi}_r/r$ (solid line), $\hat{P}/P_0$ (dashed line) and $\hat{\rho}/\rho_0$ (dot-dashed line) as a function of radial distance r/R for the fundamental sausage mode ($n = 0$) of degree $m = 1$ for three values of α: -3.2 (*top*), -2.0 (*middle*) and 0.0 (*bottom*). The displacement amplitude is $A = -0.5$. The parameters $\chi = 0.2$ and $a/R = 0.2$. The location of the internal region is indicated with thin dotted lines. The location of r_*/R, if within the plotted range, is shown as a thin dashed line. The evanescent barrier experienced by a tunneling mode is indicated with hatching. (*Right*) The same quantities for the fundamental kink mode ($n = -1$) of degree $m = 3$ with the displacement amplitude equal to $A = 0.5$ and the parameters $\chi = 0.2$ and $a/R = 0.1$.

determined by prescribing the displacement at the slab axis to be $\hat{\xi}_r(R) = RA$.

The three choices of α in Fig. 6 represent the different possible scenarios of the contribution of the loop curvature and equilibrium density advection terms to the Eulerian density perturbation in Eq. (7). The right panels show the kink mode. Depending on the value of α, the two previously mentioned terms are either in phase or out of phase with the radial displacement. Therefore, the average Eulerian density perturbation across the slab may be respectively enhanced or depleted when the loop is perturbed upwards. For $\alpha = -2$, the two terms cancel each other (see middle panel of Fig. 6). The density perturbation is then exactly equal to half the magnetic pressure perturbation. Because the magnetic pressure perturbation is approximately an anti-symmetric function of r with respect to the slab axis, the average magnetic pressure and density perturbations across the slab are approximately zero.

The above discussion is valid for the Eulerian density perturbation. However, when comparing with observations the Lagrangian description needs to be used. This shows that, independently of α, the average density is always depleted when the loop is perturbed upwards in a kink oscillation (see right panels of Fig. 7).

4.3. Efficiency of wave damping

Lateral wave leakage of vertically polarised fast magnetoacoustic oscillations is an efficient damping mechanism. Figures 8 and 9 show the quality factor of the oscillation, τ/P. Firstly, overall the oscillation quality increases with ma/R. For low degrees, both the fast sausage and kink modes have quality factors below 10, so that oscillations would damp within a few oscillation periods. In the long wavelength limit, the fast kink mode damps so quickly ($\tau/P < 1$) that the loop would not be observed to oscillate. Also, Fig. 10 shows that the damping rate increases with decreasing a/R. As a/R decreases, the phase speed of the mode increases. From Eq. (11) we see that then the width of the evanescent barrier decreases. Hence, we expect the damping rate to increase. Furthermore, the quality factor decreases with increasing χ or α (see Figs. 8 and 9). Firstly, the less density contrast a loop has, the quicker an excited oscillation will leak out into the external medium. Secondly, as α increases, the Alfvén speed profile decreases steeper with distance. Hence, the width of the evanescent barrier decreases (see Eq. (10)) and waves can more easily tunnel through the barrier and leak out into the external medium (see Fig. 10).

The damping rate tends to zero as α tends to -4 because this limit corresponds to the case studied in Paper I, for which
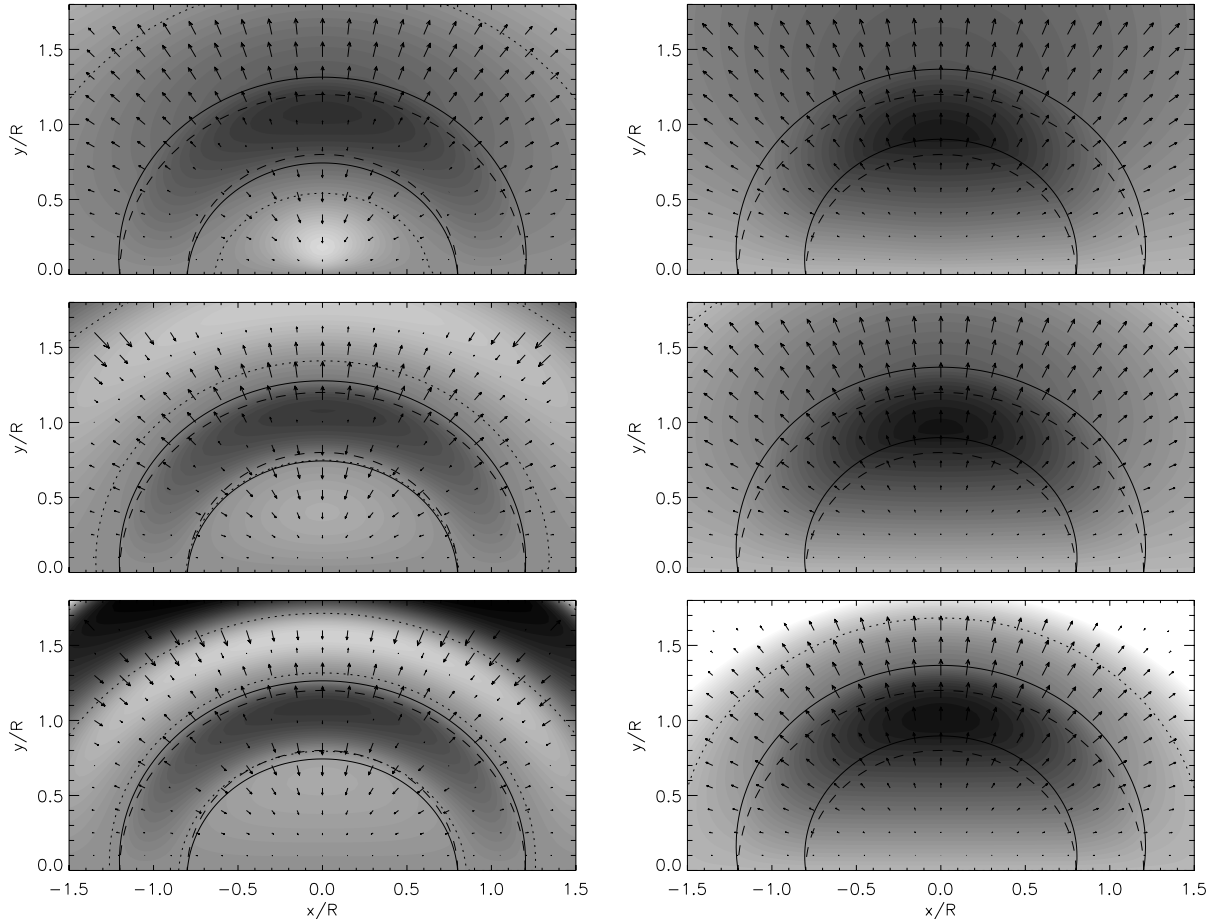
Fig. 7. (*Left*) Density perturbation $\delta\rho/\rho_0$ of the fundamental sausage mode ($n = 0$) of degree $m = 1$. for three values of α: -3.2 (*top*), -2.0 (*middle*) and 0.0 (*bottom*). The displacement amplitude is $A = -0.1$. The velocity field is overplotted. The solid (dashed) lines show the (un)perturbed position of the slab edge. The thin dotted lines show the zero contour level of the density perturbation. The parameters $\chi = 0.2$ and $a/R = 0.2$. (*Right*) Same as before but for the fundamental kink mode ($n = -1$) of degree $m = 1$ with a displacement amplitude $A = 0.2$.
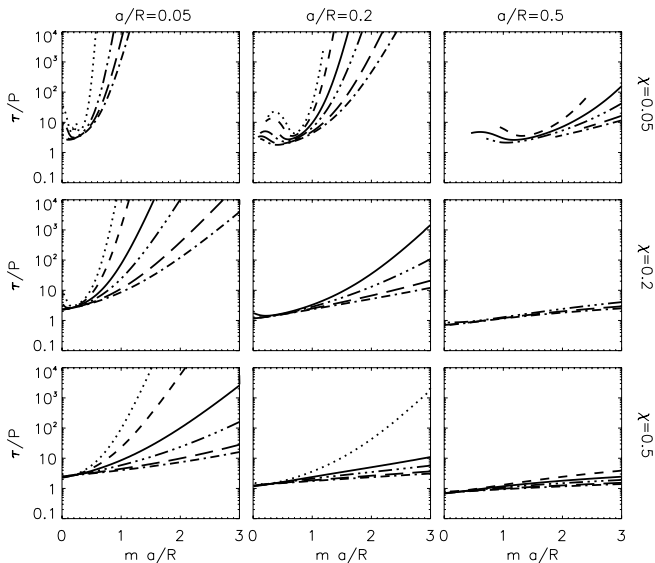

Fig. 8. Ratio τ/P as a function of ma/R for the fundamental sausage mode branch ($n = 0$) for a range of values of a/R and χ. The curves represent different values of α: -3.2 (dotted), -2.8 (dashed), -2.0 (solid), -1.2 (triple-dot dashed), 0.0 (long dashed), 0.8 (dot-dashed).

the evanescent barrier becomes infinitely thick and tunneling modes become trapped modes. With respect to leaky modes, we have to be careful in comparing the results of Paper I with the limit of α tending to -4 because the boundary condition imposed at $r = 0$ is different in the two cases.

4.4. Behaviour of leaky modes

A mode is not guaranteed to be damped quicker than higher degree modes of the same solution branch. As shown in Fig. 4, except for the fundamental kink branch, the damping rate in the leaky regime is no longer a monotonic function of ma/R but shows a number of regularly spaced extrema. Corresponding to this, a similar pattern of "wiggles" can be discerned in $\Re\Omega$ (e.g. Fig. 3).

For example, for the case shown in Fig. 4, the first five degrees ($m = 1$–5) of the second kink branch ($n = 1$) have normalised damping times of 2.44, 2.11, 1.33, 1.17 and 1.19, respectively. Of the five modes, the fourth degree mode is damped the quickest, and the lowest degree mode ($m = 1$) is damped the slowest. The number of extrema of each mode branch is given by $n + 1$. The extrema located at the smallest
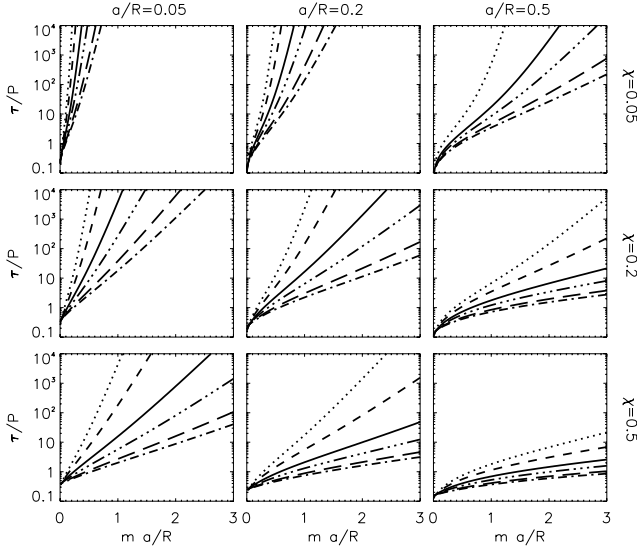
Fig. 9. Same as Fig. 8, but for the fundamental kink mode ($n = -1$).

Fig. 10. Phase speed $\Re\Omega/m$ (*top*), damping rate $\Im\Omega$ (*middle*) and quality factor τ/P (*bottom*) of the fundamental kink mode ($n = -1$) of degree $m = 1$ as a function of α for a range of values of a/R (*left to right*: 0.01, 0.05, 0.1, 0.2 and 0.5). The curves represent different values of χ: 0.01 (solid), 0.05 (dashed), 0.1 (dot-dashed), 0.2 (triple dot-dashed) and 0.5 (long-dashed).

value of m are minima (maxima) in case of a sausage (kink) mode. The extremum located at the largest real value of m is always a minimum. The values of $\Im\Omega$ at the various minima (maxima) are approximately the same and decrease with α. Also, the difference between the two extrema decreases with α, corresponding to an associated weakening of the wiggles.

In certain ranges of m, a leaky mode may appear as a tunneling mode with a lower branch number. This mixing of identity only occurs for higher solution branches and not for the fundamental kink and sausage mode solution branches. We examine this behaviour of the mode eigenfunction in detail. For this, we inspect Fig. 11. At large values of m, the waves are tunneling modes. As m decreases, the waves become leaky modes. As we pass through a pair of extrema in $\Im\Omega$, the number of internal nodes in the displacement decreases. This implies that a wave mode may have the same internal structure as a tunneling mode from a lower branch.

In particular, for sausage modes, the net effect of passing a pair of extrema is that the internal mode structure simplifies: $\Re\hat{P}$ and $\Re\hat{\xi}_r$ each lose one internal node. $\Re\hat{P}$ and $\Re\hat{\xi}_r$ each gain a node in the lower external region. This means that the internal structure of a sausage mode may resemble the internal structure of a tunneling mode (kink or sausage) with a lower branch number. However, the structure of the eigenfunctions in the lower external region would differ. The net effect for kink modes of passing a pair of extrema is not the same for all pairs (counted from large to small values of m). The net effect of odd pairs is that $\Re\hat{P}$ loses two internal nodes and $\Re\hat{\xi}_r$ loses one internal node. On the other hand, the net effect of even pairs is that $\Re\hat{P}$ maintains its number of internal nodes while $\Re\hat{\xi}_r$ loses one internal node. In both cases, $\Re\hat{P}$ and $\Re\hat{\xi}_r$ each gain a node in the lower external region. As a result, the internal structure of a kink mode may resemble the internal structure of a tunneling kink mode (but not a sausage mode) with a lower branch number.
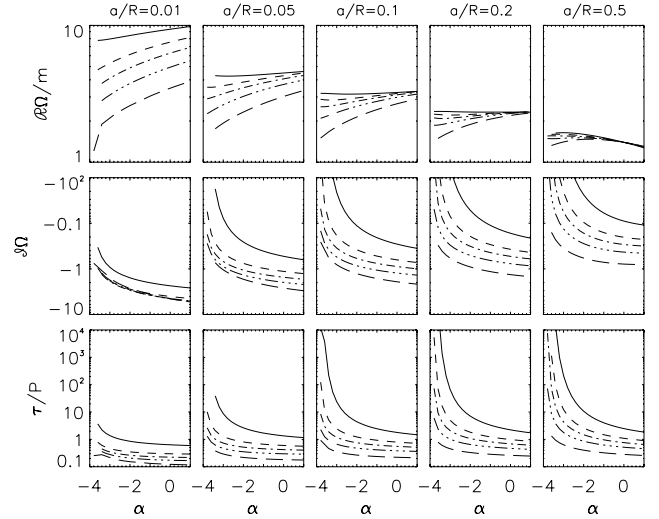
5. Wave energy leakage

How can we see from examining the wave solution, which is in the form of Bessel functions, that wave energy is leaking away from the loop and how can we distinguish between wave tunneling and straight leakage? The magnitude of the relative wave energy density is to leading order equal to $|\hat{P}/P_0|$. We shall show that, for tunneling modes, $|\hat{P}/P_0|$ is a decreasing function of r in the evanescent barrier with a minimum at r_c and is an increasing function for larger values of r. For leaky modes, $|\hat{P}/P_0|$ in the upper external region is always an increasing function of r. The increase of wave energy with r corresponds to the scenario of a wave of infinite amplitude at time $t = -\infty$ radiating energy into the external region. The increase of $|\hat{P}/P_0|$ with distance for large r represents the propagation away from the loop of a wave of decreasing energy contents. The radial gradient of the power of $|\hat{P}/P_0|$ in the upper external region is (using Eqs. (3) and (6))

$$\frac{\mathrm{d}}{\mathrm{d}r}\left|\frac{\hat{P}}{P_0}\right|^2 = -4\delta^2\left[\left((\Re\Omega)^2 - (\Im\Omega)^2\right)\chi s^2 - \nu^2\right]\frac{\mathrm{d}}{\mathrm{d}r}\left|\frac{\hat{\xi}_r}{r}\right|^2$$
$$-16\delta^2\,\Re\Omega\Im\Omega\chi s^2\,\mathcal{W}\left\{\Re\left(\frac{\hat{\xi}_r}{r}\right),\Im\left(\frac{\hat{\xi}_r}{r}\right)\right\}. \quad (15)$$

Firstly, we consider the wave solutions for large values of r (equivalent to large values of s) where $\sqrt{\chi}|\Im\Omega|s \sim O(1)$. In this regime the Hankel function is approximately equal to its asymptotic expansion

$$H_\nu^{(1)}(\sqrt{\chi}\Omega s) \approx \sqrt{\frac{2}{\pi\sqrt{\chi}\Omega s}}\,\mathrm{e}^{\mathrm{i}\left(\sqrt{\chi}\Re\Omega s - \frac{1}{2}\nu\pi - \frac{\pi}{4}\right)}\,\mathrm{e}^{-\sqrt{\chi}\Im\Omega s}. \quad (16)$$

Since $\Im\Omega < 0$, $|H_\nu^{(1)}(\sqrt{\chi}\Omega s)|$ is a decreasing function for small s and a growing function for large s. There is one minimum located at $s_* \approx -(2\sqrt{\chi}\Im\Omega)^{-1}$. Figure 12 confirms this behaviour
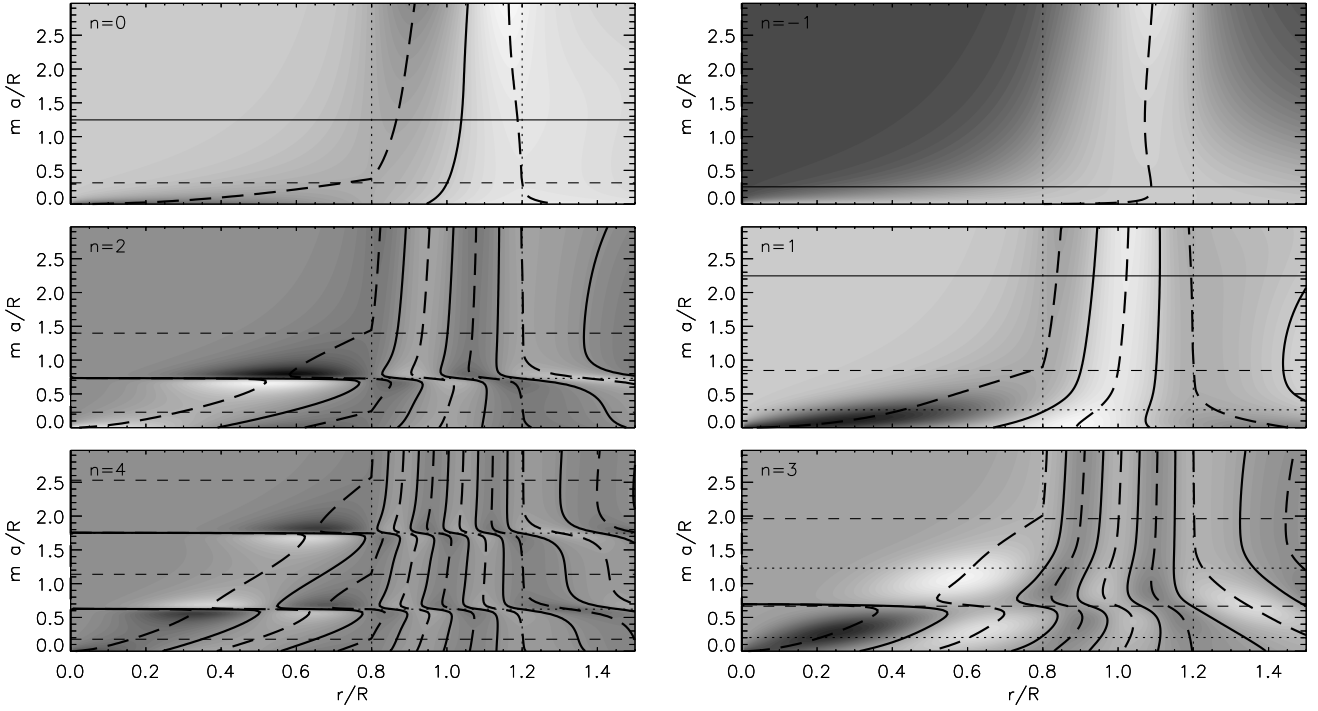
Fig. 11. (*Left*) $\Re \hat{\xi}_r / r$ as a function of r/R and ma/R for three sausage mode branches n: 0 (*top*), 2 (*middle*) and 4 (*bottom*). Solid and long-dashed curves indicate where $\Re \hat{\xi}_r / r$ and $\Re \hat{P}/P_0$ are zero respectively. A horizontal dashed (dotted) line indicates where $\Im \Omega$ has a local minimum (maximum). A horizontal solid line indicates where $V_{\mathrm{ph}}(R) = V_{\mathrm{phc}}$. The internal region is within thin vertical dotted lines. The parameters $\alpha = -2$, $\chi = 0.2$ and $a/R = 0.2$. (*Right*) The same plots for three kink mode branches n: -1 (*top*), 1 (*middle*) and 3 (*bottom*).
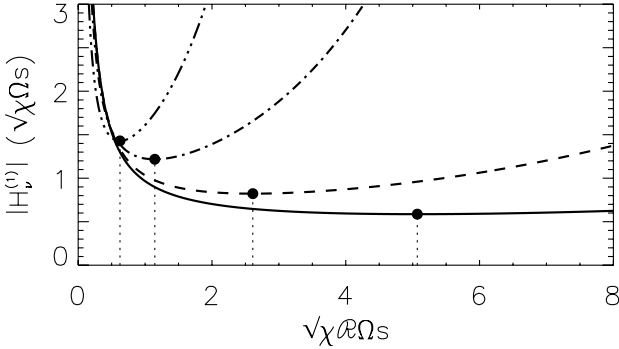

Fig. 12. Magnitude of the Hankel function of the first kind, $|H_\nu^{(1)}(\sqrt{\chi}s)|$, as a function of $\sqrt{\chi}\Re\Omega s$ for $\Im s / \Re s = -0.1$ (solid), -0.2 (dashed), -0.5 (dot-dashed) and -0.1 (triple dot-dashed). The order ν is set to unity. Locations of the minimum of the functions are marked with circles.

using the full description of $|H_\nu^{(1)}(\sqrt{\chi}\Omega s)|$ as a function of r. Using Eq. (16), Eq. (15) becomes to leading order

$$\frac{\mathrm{d}}{\mathrm{d}r}\left|\frac{\hat{P}}{P_0}\right|^2 \approx -\frac{4\delta^3}{r}\Im\Omega\,|\Omega|^2\,\chi^{3/2}s^3\left|\frac{\hat{\xi}_r}{r}\right|^2$$

$$\approx -2\sqrt{\chi}\Im\Omega\frac{\mathrm{d}s}{\mathrm{d}r}\left|\frac{\hat{P}}{P_0}\right|^2. \qquad (17)$$

This shows that the spatial rate of wave energy leakage is $\sqrt{\chi}\Im\Omega\frac{\mathrm{d}s}{\mathrm{d}r}$, which is equal to $\Im\omega/V_{\mathrm{A}}(r)$. This is consistent with a wave with a radial propagating speed equal to the Alfvén speed in the external medium, that radiates energy away from the loop at a temporal rate of $\Im\omega$.

Secondly, we consider the wave solutions in the upper external region for values of r in the vicinity of $R+a$. At this point, weak damping is assumed ($|\Im\Omega| \ll |\Re\Omega|$), which is valid in the short wavelength limit ($m \gg 1$). Equation (15) then reduces to

$$\frac{\mathrm{d}}{\mathrm{d}r}\left|\frac{\hat{P}}{P_0}\right|^2 \approx -2(\Re\Omega)^2\chi\left[\left(\frac{r}{R}\right)^{2\delta} - \left(\frac{r_c}{R}\right)^{2\delta}\right]\frac{\mathrm{d}}{\mathrm{d}r}\left|\frac{\hat{\xi}_r}{r}\right|^2. \qquad (18)$$

For weak damping, s_* is large and therefore the corresponding radial distance $r_* \gg R + a$. Hence, $\frac{\mathrm{d}}{\mathrm{d}r}|\hat{\xi}_r/r|^2$ is negative everywhere in the vicinity of $R + a$. Consequently, $|\hat{P}/P_0|$ has a minimum at r_c, the location of the upper end of the evanescent barrier (see Eq. (10)). Inside the evanescent barrier, $|\hat{P}/P_0|$ is a decreasing function of r. For values $r > r_c$, $|\hat{P}/P_0|$ is growing with r. The difference between tunneling and leaky modes is now clear. The wave energy density of a tunneling mode decreases first within the evanescent barrier, before growing with distance. This is consistent with the mechanism of leakage through wave tunneling. For a leaky mode, the evanescent barrier has zero width and therefore the wave energy density grows with distance everywhere in the upper external region.

The effective width of the evanescent barrier that a wave mode experiences becomes smaller than the width derived from geometrical considerations. This difference becomes larger as the degree m decreases (see Fig. 13).

6. Discussion and conclusions

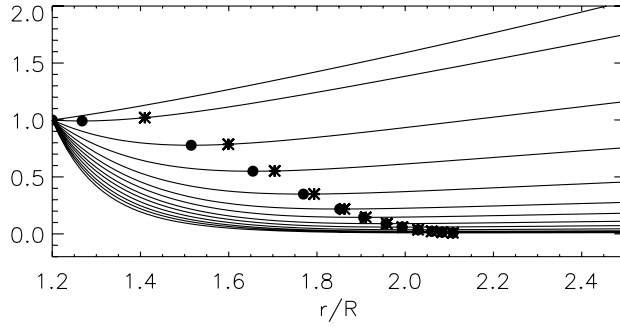We compare our results with numerical simulations by Brady & Arber (2005), who studied fast magnetoacoustic waves in a

Fig. 13. Magnitude of the magnetic pressure perturbation, $|\hat{P}/P_0|$, as a function of r, normalised by its value at $r = R + a$, for consecutive (*from top to bottom*) degrees m of the fundamental kink mode branch ($n = -1$). The locations of r_c are indicated with stars. The locations of the minimum in $|\hat{P}/P_0|$ are indicated with solid circles. The parameters $\alpha = -2.0$, $\chi = 0.2$ and $a/R = 0.2$. The location of the minimum in $|\hat{P}/P_0|$ is below r_c and this difference becomes larger as m decreases.

Fig. 14. Damping rate $\Im\Omega$ as a function of normalised period $V_{Ai}P/R$. Our analytical results are shown as circles, with the lowest degree mode visible indicated with a number. The curves are solid (dashed) where the modes are tunneling (leaky). Curves A and B correspond to $\alpha = 0.0$ and $a/R = 0.25$ & $\chi = 0.1$ and $a/R = 0.44$ & $\chi = 0.16$ respectively. Curve B is the best fit of the profile used by Brady & Arber (2005). The corresponding Alfvén speed profiles are shown in the inset. The numerical simulations by Brady & Arber (2005) are shown as diamonds, where the diamond with largest period indicates the mode of degree $m = 5$. The dashed line is a best linear fit. Brady & Arber (2005) used a curved slab model with an Epstein density profile with $a/R = 0.25$ and $\chi = 0.1$.

similar curved slab model. Brady & Arber (2005) used a continuous (Epstein) equilibrium density profile with an aspect ratio $a/R = 0.25$, and density contrast $\chi = 0.1$ (see associated Alfvén profile in inset of Fig. 14). The equivalent equilibrium density profile following Eq. (1) is with $\alpha = 0$. We have calculated the damping rate as a function of wave period for two sets of parameter values, of which one set is a best fit to Eq. (2) of the Alfvén speed profile used by Brady & Arber (2005).

Figure 14 shows that there is a good correspondence between the results of the numerical simulations by Brady & Arber (2005) and our analytical model. Any differences may be explained as follows. Firstly, we do not compare wave modes with exactly the same Alfvén speed profiles. Secondly, the numerical simulations include viscosity so that higher degree modes are expected to damp quicker than with wave leakage alone. Thirdly, the oscillations in the numerical simulations are set up by driving a footpoint and letting the system relax into a dominant oscillation mode. This introduces an uncertainty in the starting time of the mode damping. Also, due to the nature of the mode excitation, it was not possible to study the lower degree modes.

The numerical simulations by Brady & Arber (2005) and our results are complementary to explain the damping rate of the recently observed vertically polarised fast magnetoacoustic kink oscillation reported by Wang & Solanki (2004). For a loop with radius $R = 100$ Mm and cross-section radius $a = 4$ Mm, Wang & Solanki (2004) measured an oscillation period $P = 234$ s and a damping time $\tau = 714$ s. This gives a value $\tau/P = 3.05$. For such a loop we find $\tau/P = 0.2$–0.9 for a range of parameters α between -2 and 0 and $\chi = 0.1$–0.5. The reported observed quality factor is at least three times larger than the theoretically predicted value. However, considering Fig. 2 of Wang & Solanki (2004), we think that a damping time of 714 s is rather long and that a damping time even as short as 200 s may be consistent with the observational signature (Wang, private communication). Therefore, the minimum value of the quality factor from the observation is 0.85, which is closer to the theoretically predicted value. We reach the same
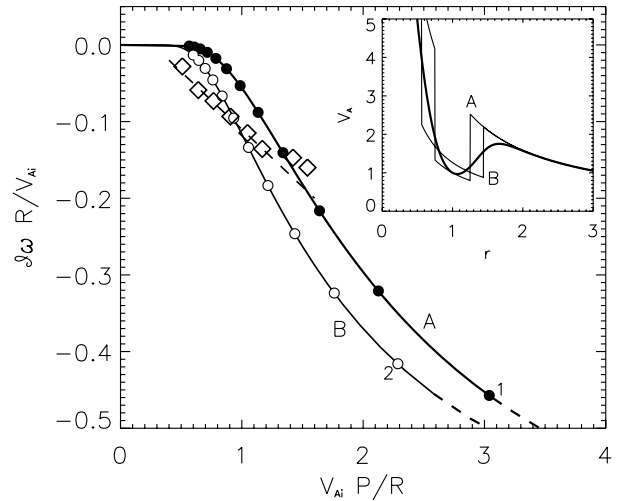
conclusion as Brady & Arber (2005) that the wave tunneling effect is a possible and efficient damping mechanism.

In straight coronal loop models, the wave solution in the external medium has the form of an exponential for a straight slab and the form of a modified Bessel function for a straight cylinder. Modified Bessel functions decay faster with distance than exponentials. Because the spatial rate of wave energy leakage is directly related to the damping rate, we expect the efficiency of lateral leakage to be decreased in cylindrical geometry compared with slab geometry. The same may be true for the damping of waves in a toroidal loop model compared with a curved slab. However, the effect of lateral leakage of waves in coronal loops in toroidal geometry remains to be investigated.

To conclude, we have shown that the propagatory behaviour of wave modes depends on the transverse equilibrium density profile, which we have modeled as a piece-wise continuous power law of index α. For a general value of $\alpha \neq -4$, trapped fast waves are not possible. Instead, waves leak into the external medium, depending whether α is larger or smaller than -4, either upwards or downwards, respectively. Based on geometric considerations as well as on the mathematical form of the wave solution, we have classified the wave modes into tunneling and leaky modes. Both types of modes leak wave energy into the external medium, but tunneling modes need to overcome an evanescent barrier. We have also studied the dependency of the damping rate on the parameters determining the transverse loop structure, showing that the damping rate increases as the density profile steepens, as the loop becomes more contrasted or as the loops becomes thinner. Also, the

assertion of Paper I that the fast kink oscillation has a non-zero density perturbation when averaged over the loop width has been confirmed. The Lagrangian density perturbation is in anti-phase with the loop displacement. Furthermore, we have shown that using the internal structure of a mode to identify its solution branch n yields different solutions depending on degree m and whether the mode is of tunneling or leaky type.

The model presented here is suited to be used for coronal seismology (see e.g. Nakariakov & Verwichte 2005), to infer from observations physical quantities such as the loop density profile, density contrast and internal Alfvén speed. Furthermore, by comparing the theory with observations, it would be possible to determine if the damping of fast magnetoacoustic oscillations is due to wave tunneling/leakage. We address the issue of coronal seismology with this model in a following publication (Verwichte et al. 2006b).
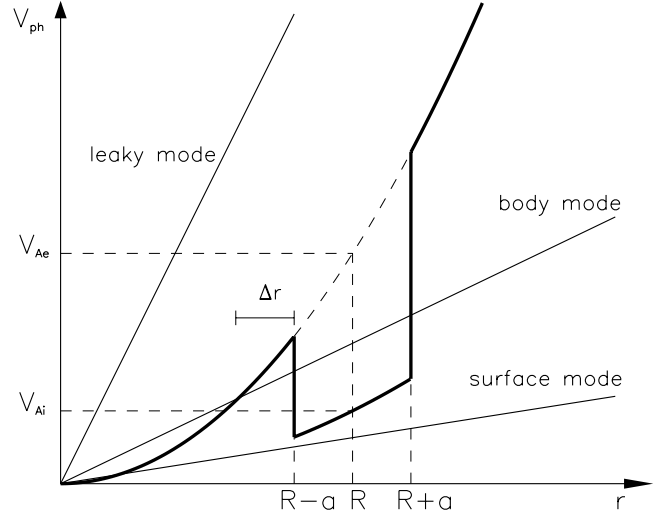
Note added in proof It was brought to our attention that A. Díaz, T. Zaqarashvili & B. Roberts recently submitted to A&A a paper, which uses the same model as presented here and in Paper I. Although they study specifically the case $\alpha = 0$ and the wave modes of degree $m = 1$ and $m = 2$, they provide similar conclusions to us, concerning the attractiveness of the mechanism of lateral wave leakage for explaining observed damping of transverse loop oscillations.

Appendix A: Inward tunneling wave modes

For values of $\alpha < -4$ ($\delta < 0$), the phase speed crosses the Alfvén speed profile from above, so that the solution is oscillatory for small r and evanescent for large r (see Fig. A.1 for an example). In this case, we impose as boundary conditions that the kinetic energy density $\rho_0 (\frac{\partial \xi_r}{\partial t})^2 / 2$ vanishes as $r \to \infty$ and we only permit the solution that propagates in the negative r-direction, away from the slab, as $r \to 0$. The solutions to Eqs. (3) and (6) for a mode of degree m that obey these boundary conditions are

$$\left(\frac{\hat{\xi}_r}{r} \right) = \begin{cases} A_e \, H_\nu^{(2)}(\sqrt{\chi}\Omega s) & r < R - a \\ A_i \, J_\nu(\Omega s) + B_i \, Y_\nu(\Omega s) & |r - R| \leq a \\ B_e \, J_\nu(\sqrt{\chi}\Omega s) & r > R + a, \end{cases} \quad (A.1)$$

Fig. A.1. Alfvén speed profile as a function of r, corresponding to Eq. (2) with $\alpha = -6$. The phase speeds of three wave scenarios corresponding to surface, body and leaky modes are shown.

$$\left(\frac{\hat{P}}{P_0} \right) = -2r \begin{cases} A_e \, \frac{\mathrm{d}}{\mathrm{d}r} H_\nu^{(2)}(\sqrt{\chi}\Omega s) & r < R - a \\ A_i \, \frac{\mathrm{d}}{\mathrm{d}r} J_\nu(\Omega s) + B_i \, \frac{\mathrm{d}}{\mathrm{d}r} Y_\nu(\Omega s) & |r - R| \leq a \quad (A.2) \\ B_e \, \frac{\mathrm{d}}{\mathrm{d}r} J_\nu(\sqrt{\chi}\Omega s) & r > R + a, \end{cases}$$

where $H_\nu^{(2)}$ is the second Hankel function of order ν. Continuity of $\hat{\xi}_r$ and the Lagrangian total pressure perturbation, $\delta \hat{P} = \hat{P} - 2P_0 \hat{\xi}_r / r$, at $r = R \pm a$ leads to the dispersion relation

$$\frac{\mathcal{W}\left\{ J_\nu(\Omega s_-), H_\nu^{(2)}(\sqrt{\chi}\Omega s_-) \right\}}{\mathcal{W}\left\{ Y_\nu(\Omega s_-), H_\nu^{(2)}(\sqrt{\chi}\Omega s_-) \right\}} = \frac{\mathcal{W}\left\{ J_\nu(\Omega s_+), J_\nu(\sqrt{\chi}\Omega s_+) \right\}}{\mathcal{W}\left\{ Y_\nu(\Omega s_+), J_\nu(\sqrt{\chi}\Omega s_+) \right\}} \cdot (A.3)$$

References

Brady, C. S., & Arber, T. D. 2005, A&A, 438, 733
Brady, C. S., Verwichte, E., & Arber, T. D. 2006, A&A, 449, 389
Edwin, P. M., & Roberts, B. 1982, Sol. Phys., 76, 239
Edwin, P. M., & Roberts, B. 1983, Sol. Phys., 88, 179
Nakariakov, V. M., & Verwichte, E. 2005, Living Rev. Solar Phys., 2, 3, URL (2005-07-05)
   http://www.livingreviews.org/lrsp-2005-3
Roberts, B., Edwin, P. M., & Benz, A. O. 1984, ApJ, 279, 857
Verwichte, E., Foullon, C., & Nakariakov, V. M. 2006a, A&A, 446, 1139
Verwichte, E., Foullon, C., & Nakariakov, V. M. 2006b, A&A, submitted
Wang, T. J., & Solanki, S. K. 2004, A&A, 421, L33